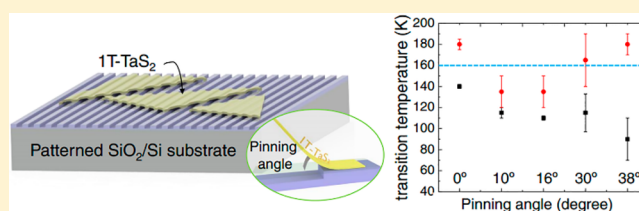


Tuning Phase Transitions in 1T-TaS<sub>2</sub> via the SubstrateRui Zhao,<sup>†,‡</sup> Yi Wang,<sup>†,§</sup> Donna Deng,<sup>†,‡</sup> Xuan Luo,<sup>§</sup> Wen Jian Lu,<sup>§</sup> Yu-Ping Sun,<sup>§,||,⊥</sup> Zi-Kui Liu,<sup>†</sup> Long-Qing Chen,<sup>†</sup> and Joshua Robinson<sup>\*,†,‡,§</sup><sup>†</sup>Department of Materials Science and Engineering and <sup>‡</sup>The Center for 2-Dimensional and Layered Materials, The Pennsylvania State University, University Park, Pennsylvania 16802, United States<sup>§</sup>Key Laboratory of Materials Physics, Institute of Solid State Physics and <sup>||</sup>High Magnetic Field Laboratory, Chinese Academy of Sciences, Hefei 230031, People's Republic of China<sup>⊥</sup>Collaborative Innovation Centre of Advanced Microstructures, Nanjing University, Nanjing 210093, People's Republic of China

## Supporting Information

**ABSTRACT:** Phase transitions in 2D materials can lead to massive changes in electronic properties that enable novel electronic devices. Tantalum disulfide (TaS<sub>2</sub>), specifically the “1T” phase (1T-TaS<sub>2</sub>), exhibits a phase transition based on the formation of commensurate charge density waves (CCDW) at 180 K. In this work, we investigate the impact of substrate choice on the phase transitions in ultrathin 1T-TaS<sub>2</sub>. Doping and charge transfer from the substrate has little impact on CDW phase transitions. On the contrary, we demonstrated that substrate surface roughness is a primary extrinsic factor in CCDW transition temperature and hysteresis, where higher roughness leads to smaller transition hysteresis. Such roughness can be simulated via surface texturing of SiO<sub>2</sub>/Si substrates, which controllably and reproducibly induces periodic strain in the 1T-TaS<sub>2</sub> and thereby enables the potential for engineering CDW phase transitions.

**KEYWORDS:** 1T-tantalum disulfide (1T-TaS<sub>2</sub>), phase transition, Raman spectroscopy, substrate impact, strain



Electron–electron and electron–phonon coupling are well-known phenomena in materials with highly anisotropic band structures.<sup>1</sup> Such coupling can lead to singlet and triplet superconductivity,<sup>2</sup> spin-density waves (SDW),<sup>3,4</sup> and charge density waves (CDW).<sup>5–7</sup> One particular group of low-dimensional materials, transition metal dichalcogenides (TMDs), are among the most recognized CDW materials. Among them, group-V TMDs (e.g., tantalum disulfide (TaS<sub>2</sub>), tantalum diselenide (TaSe<sub>2</sub>), and titanium disulfide (TiS<sub>2</sub>)) exhibit unique electronic and structural properties. The 1T-TaS<sub>2</sub> is particularly interesting because it possesses CDW and Mott insulator phenomenon.<sup>8,9</sup> Undistorted 1T-TaS<sub>2</sub> is stable at high temperatures and adopts a layered structure with each layer held together via van der Waals forces. Within each layer, Ta atoms are octahedrally bonded to six sulfur atoms. Below 540 K, 1T-TaS<sub>2</sub> distorts into an incommensurate CDW (ICCDW) phase where the atoms shift slightly from their original positions and are no longer commensurate to the original lattice. At 350 K, a nearly commensurate CDW (NCCDW) phase is formed with partial structures being commensurate to the original lattice. When further decreasing to below 180 K, a commensurate CDW (CCDW) phase becomes stable, where all Ta atoms form a superstructure that is fully commensurate with the original lattice structure.<sup>10</sup> This superstructure assumes a  $\sqrt{13} \times \sqrt{13}$  David star and has a wave vector of  $[q_t = (3G_t - G_i)/13]$ . The David star consists of 13 Ta atoms with two groups of 6 Ta atoms centered on 1 Ta atom. Through this NCCDW/CCDW (NC/C) transition,

metallic 1T-TaS<sub>2</sub> becomes “insulating” with a small band gap ( $\sim 0.2$  eV).<sup>11</sup> DiSalvo and Graebner suggest that the resistivity increase during the NC/C transition is due to variable range hopping,<sup>12</sup> while Fazekas and Tosatti propose a Mott phase transition as the primary mechanism for the resistance change.<sup>11</sup> Furthermore, there are a wide variety of theoretical works conducted to model the CDW transitions in these materials in attempts to elucidate the transition mechanisms.<sup>13,14</sup>

Both electronic<sup>15</sup> and optical<sup>16</sup> methods have been used to drive phase transitions in correlated systems. Additionally, doping with iron or selenium can induce a superconducting phase in 1T-TaS<sub>2</sub>.<sup>17,18</sup> While the application of a high external pressure (above  $\sim 0.8$  GPa) inhibits CCDWs,<sup>10</sup> an in-plane compressive strain from the supporting substrate (calcium fluoride, CaF<sub>2</sub>) helps stabilize the CCDW, resulting in a 20–30 K higher transition temperature.<sup>19</sup> Successful device applications based on the 1T-TaS<sub>2</sub> phase changes use mostly SiO<sub>2</sub>/Si substrates<sup>20</sup> but one must be careful that H<sub>2</sub>O or O<sub>2</sub> adsorption on the SiO<sub>2</sub> surface does not impact the 1T-TaS<sub>2</sub> phase transition.<sup>21</sup> Regardless of external stimuli, it is clear that film thickness may become an obstacle to monolayer metal–insulator transitions (MIT) in 1T-TaS<sub>2</sub>.<sup>22</sup> Theoretically, interlayer interactions play a very important role in the Mott

Received: January 30, 2017

Revised: April 26, 2017

Published: May 2, 2017

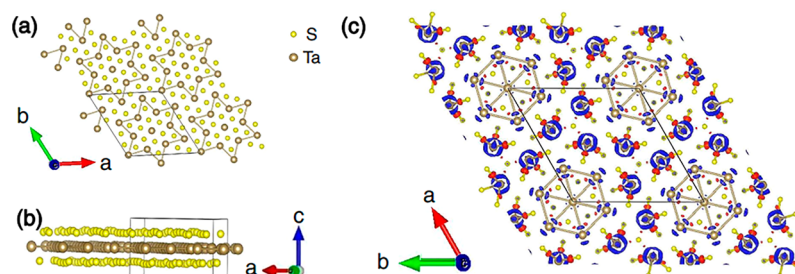


**Figure 1.** (a) Structure of 1T-TaS<sub>2</sub> in CCDW phase. New superstructures are formed, adopting the shape of “David star”. Five ranges of Ta–Ta bonds are detected and indicated with numbers (b) the side view of 1T-TaS<sub>2</sub> in the CCDW phase. As Ta adopts the new structure, rigid Ta–S bonds lead to upward- and downward- bending of S atoms. (c) The calculated charge loss and gain in and of 1T-TaS<sub>2</sub>, which are in the CCDW phase. The blue isosurface represents an electron loss of 20 electron/nm<sup>3</sup>, the red isosurface represents an electron gain of 20 electron/nm<sup>3</sup>.

phase transitions,<sup>23,24</sup> where interlayer interactions weaken as the number of layers is reduced.<sup>25</sup> It is predicted that the CCDW phase in 1T-TaS<sub>2</sub> flakes thinner than 13 layers is no longer stable.<sup>26</sup>

Substrates play an important role in the intrinsic properties of 2D materials during synthesis. This is evident with the synthesis of graphene, where the choice of substrate can lead to different degrees of charge transfer and may also induce mechanical instability that leads to variation in carrier mobility and can be detrimental to device processing.<sup>27</sup> Furthermore, strain-induced phenomena due to substrate lead to modification of the bandgap,<sup>28</sup> including indirect-to-direct band gap transitions,<sup>29</sup> modulation in the optical band gap, and introduction of magnetism.<sup>30</sup> This has led to strain engineering in 2D materials, generating a variety of promising property changes.<sup>31–34</sup> To understand the effects of common substrates on NC/C transitions of ultrathin 1T-TaS<sub>2</sub>, we focus on the phase transitions of both 8.8 and 18 nm 1T-TaS<sub>2</sub> flakes through a series of Raman studies. By comparing transition temperatures of 1T-TaS<sub>2</sub> with similar thickness on different substrates (Si/SiO<sub>2</sub>, sapphire, epitaxial graphene (eG), vanadium oxide (VO<sub>2</sub>), and strontium vanadium oxide (SVO)), we demonstrate that surface texture (roughness) is the primary influence on CDW transitions and can be used to manipulate the NC/C phase transition in nanometer thick 1T-TaS<sub>2</sub> layers.

The 1T-TaS<sub>2</sub> single crystals<sup>35</sup> with different thicknesses are exfoliated onto a variety of substrates to better understand the impact of substrate on the CCDW phase stability. Several works indicate that thin 1T-TaS<sub>2</sub> flakes (below 13 layers) will no longer exhibit the CCDW phase<sup>36,22</sup> and hence we choose the layer thicknesses of ~18 nm to ensure that the NC/C transition is preserved. In addition to the above-mentioned substrates, we also utilize patterned SiO<sub>2</sub> surfaces (see [Supporting Information](#) for fabrication process) to understand the role of substrate roughness and structural periodicity in the CCDW stability. Numerous tools were applied to characterize the phase transitions in these materials with Raman spectroscopy being the primary guide for understanding the phase stability of TaS<sub>2</sub> on different substrates. Raman spectroscopy is a powerful technique to detect the NC/CCDW phase transition,<sup>37</sup> where peaks associated with CCDW phase appear when the transition occurs.<sup>36</sup> Atomic force microscopy (AFM) was used to identify the morphology and thickness of desired 1T-TaS<sub>2</sub> flakes with similar thicknesses on different substrates. Samples are stored in a nitrogen glovebox after exfoliation to minimize potential oxidation. Low-temperature Raman spectroscopy was conducted to detect the phase transitions. The HFS600 Heating and Freezing Stage from Linkam Scientific

Instruments was used to lower sample temperature to that of liquid nitrogen (LN). The cooling and heating rates were controlled to below 2 K/min. Raman spectra were collected using a Horiba LabRAM HR Evolution Raman spectrometer. For all Raman spectroscopic measurements, 488 nm Ar ion laser and 1800/mm grating were used. The laser power and integration time are minimized to avoid potential heating of the TaS<sub>2</sub>. First-principles calculations were performed on the “Star-of-David” clusters<sup>36</sup> in which the atoms are arranged in a hexagonal stacking with neighboring layers aligned directly atop each other. The smallest primitive unit cell contains 39 atoms. The projector-augmented wave (PAW) method<sup>38,39</sup> implemented in the Vienna ab initio simulation package (VASP, version 5.3) together with the Perdew–Burke–Ernzerhof (PBE)<sup>40</sup> exchange-correlation function was employed.

In the CCDW phase, periodic lattice distortions and CDWs occur simultaneously.<sup>41</sup> The 1T-TaS<sub>2</sub> transitions into the new CCDW superstructure at low temperatures was previously verified using X-ray diffraction (XRD).<sup>42</sup> We use pseudopotentials with Ta 5p<sup>6</sup>6s<sup>2</sup>5d<sup>3</sup> and S 3s<sup>2</sup>3p<sup>6</sup> shells as valence states ([Figure 1](#)). Lattice optimization was performed at the fixed cell volume of 0.7536 nm<sup>3</sup>. Both cell shape and internal atomic positions were relaxed, using a  $\Gamma$ -centered  $4 \times 4 \times 7$  *k*-mesh and an energy cutoff of 336.7 eV, until the total electronic energy reached a convergence threshold of 10<sup>−8</sup> eV. It is observed that the CDW transition resulted in the Ta–Ta bond length change from an average 0.34 nm to the minimum length of 0.32 nm within the center of the “Star-of-David” cluster and to the maximum length of 0.35 nm connecting the neighboring “Star-of-David” clusters ([Figure 1a](#)). There are five ranges of bond length that resulted from the structure change as indicated in the diagram. The bond length changes and ranges are well correlated with the X-ray diffraction measurements.<sup>42</sup> It is also noticed that both top-layer sulfur plane and bottom-layer sulfur plane are no longer flat ([Figure 1b](#)) and move either away or toward the middle Ta planes while the Ta plane remains unchanged. This is most likely because the CDW phase transitions are dominated by the Ta–Ta electronic coupling. When Ta atoms move and form the new superstructure, rigid Ta–S bonds will force S atoms to move in either up or down direction to accommodate the new structure. As a result, S atoms no longer lie along a straight line or within a flat plane. Furthermore, we evaluate the electronic charge distribution due to the CDW transition by perturbing the atomic positions in the middle TaS<sub>2</sub> layers of a  $1 \times 1 \times 3$  superstructure of the optimized structure.<sup>43</sup> The calculated charge loss and gain relative to those of the free atoms are plotted in [Figure 1c](#). It shows that the electron loss is mainly from the outer Ta atom

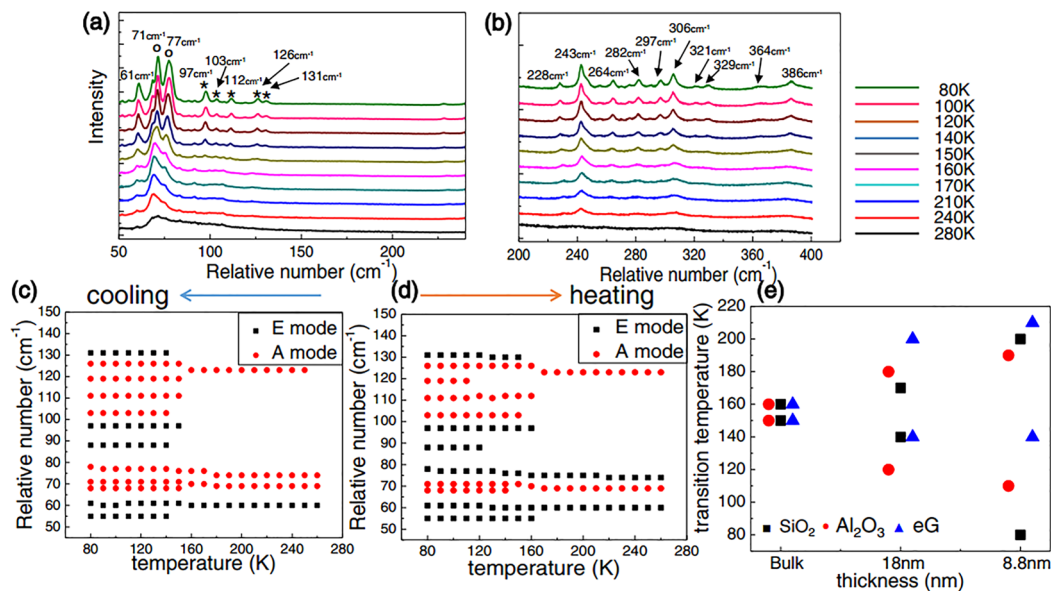


**Figure 2.** Exfoliated 1T-TaS<sub>2</sub> on common substrates as a function of thicknesses (a) lower range (50–150 cm<sup>-1</sup>) and (b) higher range (220–350 cm<sup>-1</sup>) of phonon modes of 1T-TaS<sub>2</sub> as a function of temperature. Stars indicate new peaks at the CCDW phase, while circles indicate main peak split-up when NC/C transition occurs. Phonon modes evolution with temperature when (c) cooling to LN temperature and (d) heating from LN temperature. (e) Transition temperatures of bulk, 18 nm, and 8 nm flakes exfoliated on SiO<sub>2</sub>, sapphire and eG substrates.

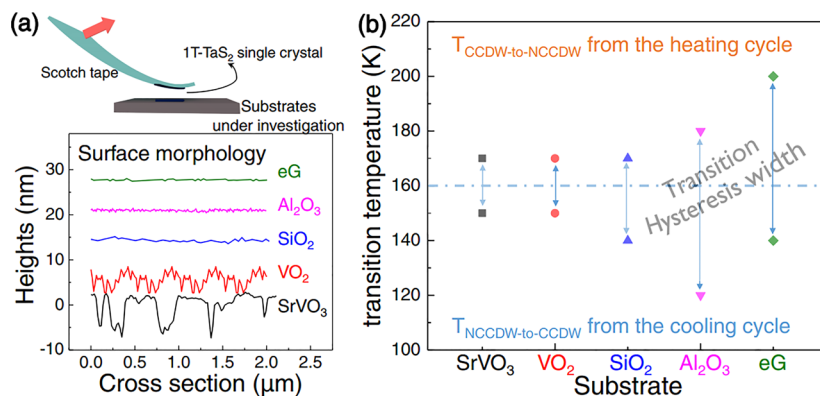


**Figure 3.** (a) Top figure is a demonstration of mechanical exfoliation of 1T-TaS<sub>2</sub> onto various substrates, bottom diagram demonstrates substrate morphology of different substrates measured by atomic force microscopy illustrates the wide variety of surface roughness across the substrate choices. (b) The 1T-TaS<sub>2</sub> of thickness 18 nm on five different substrates show NC/CCDW phase transitions in both cooling curves and heating curves. The transition temperatures are recorded based on their Raman feature evolutions.

ring of “Star of David” cluster, which are subsequently accumulated at the inner Ta–S bond.

Raman spectroscopy is ideal for understanding the substrate impact on the exfoliated 1T-TaS<sub>2</sub> phonon vibrations and CDW transitions from room temperature to 77 K. Figure 2a,b shows a representative series of nonpolarized Raman spectra from bulk 1T-TaS<sub>2</sub>. Wavenumbers <150 cm<sup>-1</sup> (Figure 2a) are related with tantalum atom movements while phonon modes within 220–320 cm<sup>-1</sup> (Figure 2b) are more associated with sulfur atoms.<sup>44</sup> The transformation from NCCDW to CCDW at approximately 140–150 K is identified by the formation of new Raman peaks below 150 cm<sup>-1</sup>. Two major Raman spectral changes are peak splitting (originally one peak at 70 cm<sup>-1</sup>) and new peaks appearing at approximately 100 cm<sup>-1</sup>. The latter one is proposed to result from acoustic modes folding back to the  $\Gamma$ -point upon the NC/C transition.<sup>36</sup> Raman spectra is collected in both cooling and heating cycles (Figure 2c,d). In this case, we focus on the existence of the well-resolved peaks near 100

cm<sup>-1</sup> to represent the NC/C transition, which also enables the observation of a phase transition hysteresis.

The substrate choice can have significant impact on the NC/C transition temperature and hysteresis. This is evident when comparing various exfoliated 1T-TaS<sub>2</sub> flakes with similar thickness on sapphire (Al<sub>2</sub>O<sub>3</sub>), SiO<sub>2</sub>/Si, and graphene (eG) substrates (Figure 2e). For 1T-TaS<sub>2</sub> with thicknesses above 500 nm, the Raman evolution is independent of substrate choice, suggesting that “thick” flakes mimic bulk 1T-TaS<sub>2</sub> with little impact from the substrate. Furthermore, the temperature (*T*) hysteresis is small ( $\Delta T \sim 10$  K), different from electrical measurements, which exhibit a temperature hysteresis of 50 K.<sup>45</sup> We assume that the dynamics of CDW domains driven by electric means may be more sensitive to local deformations<sup>46</sup> and show a more “sluggish” result than vibrational Raman spectra.<sup>47</sup> When the flake thickness is decreased there is a significant change of the transition temperature, and broadening of the hysteresis even though the average of the transitions remain in between 140 and 150 K.<sup>22</sup> The transition



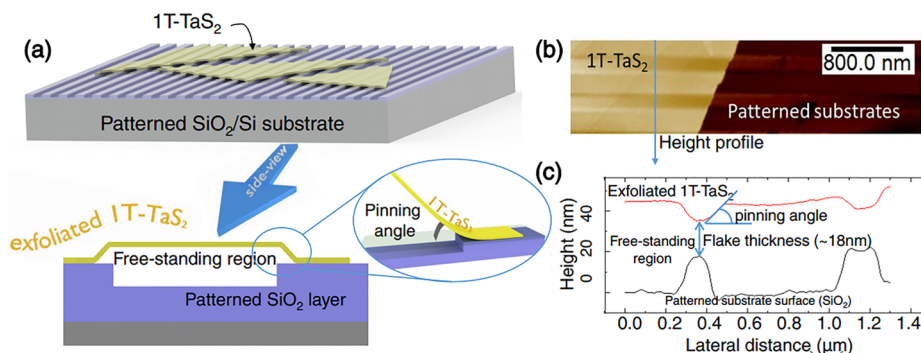


**Figure 4.** (a) Schematic figure demonstrating 1T-TaS<sub>2</sub> (about 18 nm thickness) exfoliated onto the patterned SiO<sub>2</sub>/Si substrates. The side view and inset figures include more details about the pinning angles (b) AFM figure of the exfoliated 1T-TaS<sub>2</sub> on the patterned substrate. (c) The diagram showing the morphology of both exfoliated 1T-TaS<sub>2</sub> and patterned substrate.

temperature and hysteresis modifications as a function of reduced thickness indicate that the stress in the films may play a role. It has been reported that a high intrinsic stress impacts both transition temperatures and hysteresis width.<sup>48</sup> Although the  $\Delta T$  is similar for 8 nm flakes on both sapphire and eG substrates, the average transition temperature is  $\sim 15$  K higher in flakes on eG substrates. We hypothesize that this is due to electron doping 1T-TaS<sub>2</sub> from the graphene. First principle calculations indicated that carrier doping can influence the CDW structure in both monolayer and bulk form of 1T-TaS<sub>2</sub>,<sup>49</sup> which could lead to higher transition temperatures found in 8 nm flakes exfoliated on eG versus SiO<sub>2</sub>.

Substrate surface roughness also affects CDW transition temperature and hysteresis ( $\Delta T$ ). This is evident when comparing 18 nm thick exfoliated flakes on substrates of varying roughness and conductivity (Figure 3). In the case of electronic properties of the substrate, there is no clear trend related to the conductivity, indicating that doping or charge transfer from the substrate is negligible for the 18 nm flakes. However, if one compares the NC/CCDW transition on substrates with different surface roughness, it becomes clear that surface morphology can have a significant impact. Comparing surface morphology (Figure 3a), VO<sub>2</sub> and SVO exhibit the highest surface roughness and have the largest peak-to-valley ratio, whereas SiO<sub>2</sub>/Si, sapphire, and eG exhibit increasingly smaller surface roughness, respectively. Interestingly, hysteresis in the phase transition is inversely proportional to roughness (Figure 3b). This suggests that the source of the transition temperature hysteresis is a function of the substrate/TaS<sub>2</sub> interface, and the mechanical impact on the formation of CCDW, where those samples with partially suspended TaS<sub>2</sub> exhibit higher transition temperatures and smaller hysteresis. This phenomenon is similar to that reported for suspended monolayer MoS<sub>2</sub>, where periodic interactions with the substrate are enough to drive structure changes in the layer. This also leads to slight modifications in the MoS<sub>2</sub> band structure following an intraplane distance modification.<sup>50</sup>

To further understand the substrate impact, we design a nanotextured surface in SiO<sub>2</sub>/Si that nominally mimics the fraction of suspended versus supported 1T-TaS<sub>2</sub> flakes that occur in the rough VO<sub>2</sub> and SVO substrates. Figure 4a schematically demonstrates the patterning process, where exfoliated 18 nm thick flakes of 1T-TaS<sub>2</sub> span a series of trenches. The side view (Figure 4a) schematically demonstrates how the exfoliated TaS<sub>2</sub> is curved on the patterned substrates

with the highest curvature occurring at the mesa edge. Figure 4b is an AFM micrograph showing a 1T-TaS<sub>2</sub> flake on a textured surface with 400 nm SiO<sub>2</sub> mesas separated by 400 nm trenches. Figure 4c is a cross section of the SiO<sub>2</sub> substrate and of a 1T-TaS<sub>2</sub> flake on the textured SiO<sub>2</sub> demonstrating that, contrary to what was expected, the suspended portion of the flake has a positive curvature (bows upward). This is the case in all samples tested, and it is hypothesized that the suspended flakes experience a positive vertical force (pulling) during the exfoliation process. Regions of the flake that are suspended subsequently lift up at the center, causing a positive curvature in the flakes. As a result, the SiO<sub>2</sub> mesas are believed to serve as pinning centers. On the basis of the peeling process, the upward bulging flakes can be differentiated by their “pinning angle” ( $\tan \theta$ ), which is the ratio of bow height ( $h$ ) to the horizontal length ( $l$ ) of the suspended region. Starting from one pinning center, the exfoliated flakes curve upward first and then become suspended at the middle top and then curves back to the next pinning center, which induces nonuniform strain across the flakes. In our case, the strain is inversely related with the radius of curvature according to  $\epsilon = (t/2)/(R - t/2) + \epsilon_{\text{add}}$ , where  $\epsilon$  is the bending strain,  $t$  is sample thickness,  $R$  is the radius of curvature, and  $\epsilon_{\text{add}}$  is the additional residue strain.<sup>51</sup>

Transport and spectroscopy studies on static and dynamic properties of CDW states<sup>52,53</sup> suggest “pinning” can be used to describe the strength of the interactions between CDW states and impurities or other external stimuli. Here, we find that pinning angle (the angle between the TaS<sub>2</sub> flake and substrate post exfoliation) (Figure 4a inset) has a large impact on the NC/C phase transition temperature and transition hysteresis. The 1T-TaS<sub>2</sub> that curves upward from the pinning center (the point where flake leaves the substrate surface) undergoes a mix of tensile and compressive strain that subsequently frustrates the typical CDW modulations.<sup>54</sup> On the basis of the correlation between the sample morphology change at the pinning center (mesa in the substrates) and the corresponding transition temperatures measured from Raman spectroscopy (Figure 5a), the pinning angle at the sample-mesa contact region may play a dominating role in the NC/C phase transitions. Compared with the pristine SiO<sub>2</sub>/Si surface (pinning angle = 0°), smaller pinning angles (both 10° and 16°) are shown to induce the CCDW phase at a slightly lower temperature and with a  $\Delta T$  of 25–40 K. This indicates that smaller pinning angles, and thereby larger radius of curvature, will globally shift the transition temperature to lower values without impacting  $\Delta T$ . In other words, small pinning angles can correspond to weak

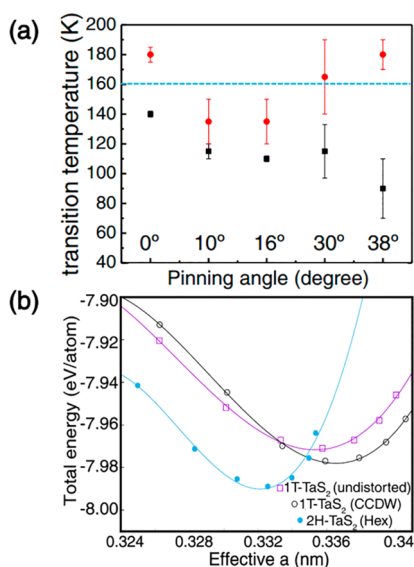


**Figure 5.** (a) NC-to-CCDW transition temperatures of  $\sim 18$  nm 1T-TaS<sub>2</sub> on the patterned substrates based on their Raman evolution and pinning angle by the patterned substrates. (b) DFT calculation on the comparison of the total energies on undistorted 1T-TaS<sub>2</sub>, 1T-TaS<sub>2</sub> in the CCDW phase and undistorted 2H-TaS<sub>2</sub>.

pinning forces, which is believed to partition the CDW phases into constant-phase regions.<sup>55</sup> As a result, the CDW states are still collective;<sup>56</sup> however, the energy required for the phase transition is larger due to the additional potential energy resulting from strain-induced pinning. Therefore, the transition temperatures for NC/CCDW transition in both the cooling and heating cycles are lowered. Once the pinning angle increases ( $\geq 30^\circ$  in this study), the induced strain from the smaller radius of curvature leads to strong pinning forces that control the CCDW phase transition at these “high strain points”.<sup>55</sup> In our case, the highest strain energy is confined to the curved region, which can frustrate the phase transition throughout the entire flake. On the basis of Raman spectroscopy (Figure 5a), the transition  $\Delta T$  increases dramatically to nearly 90 K at the highest pinning angle ( $38^\circ$ ). Such an increase in hysteresis indicates a higher energy barrier to transform from one phase to another phase. This ultimately requires decreasing the temperature to  $<90$  K (versus 140 K) before the NC/C transition occurs during cooling, and  $>180$  K (versus 140 K) for the C/NCCDW transition.

Density functional theory (DFT) indicates that in-plane strain can effect phase stability in 1T-TaS<sub>2</sub>. Comparing the total energy of commensurate phase (CCDW) 1T-TaS<sub>2</sub> with that of both undistorted 1T-TaS<sub>2</sub> (the stable phase at high temperature) and 2H-TaS<sub>2</sub> (Figure 5b) indicates that the CCDW phase can be made stable via in-plane tensile strain. Above all, in the high pinning force case (large pinning angle) the NCCDW  $\rightarrow$  CCDW phase transition is frustrated during the cooling cycles, which can be related with higher energy barriers at the mesa edge and the curved regions. However, once the CCDW phase is formed, the commensurate phase structure is now locked into place and needs a higher energy to initiate the atom movements and go back to the nearly commensurate phase.<sup>57</sup> As a result, a large  $\Delta T$  is observed for both  $30^\circ$  and  $38^\circ$  pinning angles (Figure 5a). On the other hand, for the smaller pinning angles ( $10^\circ$  and  $16^\circ$ ), lower transition temperatures during cooling cycles also occur, but these small

pinning angles do not “lock” the commensurate phase and may ultimately serve as a “nucleation point” for the CCDW  $\rightarrow$  NCCDW transition. Thus, a much smaller  $\Delta T$  (Figure 5a) results. This is similar to that found for those samples with higher roughness (SVO and VO<sub>2</sub>), where we actually see a decrease in hysteresis compared to the lower roughness SiO<sub>2</sub>, sapphire, and graphene. In addition to enhanced hysteresis and average temperature change, we also note more scatter in data associated with larger pinning angles. This result can be correlated with the fact that large disruption in the pristine 1T-TaS<sub>2</sub> structure will hinder phase transitions (regardless of heating/cooling). However, different than structural disruption by doping or intercalation, which can preclude the CCDW phase and is not usually controllable, the patterned substrates may help stabilize CCDW structures toward a higher temperature as indicated by the transition temperatures in the heating cycles.

We have demonstrated that substrate impact on the NC/CCDW phase transitions in ultrathin ( $<20$  nm) 1T-TaS<sub>2</sub> can be significant. We observed that the surface morphology dominates the transition behavior and confirm this via patterning of SiO<sub>2</sub>/Si substrates to engineer the surface strain and to control the phase transition using the “pinning angle”, related to locally induced strain. It has been found that the phase transition largely depends on the pinning center and the pinning force. The metastable CCDW phase can survive to higher temperatures at larger pinning angles (above  $30^\circ$ ). This strain-engineered increase in the NC/C phase transition hysteresis is the first step in fully understanding how surface engineering can tune the properties of 2D-CDW materials. Most importantly, the quasi-stable CCDW phase near room temperature is promising for a variety of electronic applications.<sup>20,58</sup>

## ■ ASSOCIATED CONTENT

### § Supporting Information

The Supporting Information is available free of charge on the ACS Publications website at DOI: 10.1021/acs.nanolett.7b00418.

Additional information and figures (PDF)

## ■ AUTHOR INFORMATION

### Corresponding Author

\*E-mail: jrobinson@psu.edu.

### ORCID

Yi Wang: 0000-0001-6154-945X

Joshua Robinson: 0000-0001-5427-5788

### Notes

The authors declare no competing financial interest.

## ■ ACKNOWLEDGMENTS

This work was supported by NSF Grant EFRI-1433307. The authors acknowledge L. Zhang for SrVO<sub>3</sub> substrates and H. T. Zhang for VO<sub>2</sub> substrates. Y.W. and L.Q.C. acknowledge the financial support by U.S. Department of Energy, Office of Basic Energy Sciences, Division of Materials Science and Engineering under Award FG02-07ER46417. Synthesis of 1T-TaS<sub>2</sub> was supported by the National Key Research and Development Program (2016YFA0300404), the National Nature Science Foundation of China (11674326), the Joint Funds of the National Natural Science Foundation of China, the Chinese

Academy of Sciences' Large-Scale Scientific Facility (U1232139, U1432139), and Key Research Program of Frontier Sciences of CAS (QYZDB-SSW-SLH015).

## REFERENCES

- (1) Gruner, G. The dynamics of charge-density waves. *Rev. Mod. Phys.* **1988**, *60*, 1129–81.
- (2) Maeno, Y.; Rice, T. M.; Sigrist, M. The intriguing superconductivity of strontium ruthenate. *Phys. Today* **2001**, *54*, 42–7.
- (3) Rotter, M.; Tegel, M.; Johrendt, D.; Schellenberg, I.; Hermes, W.; Pottgen, R. Spin-density-wave anomaly at 140 K in the ternary iron arsenide BaFe<sub>2</sub>As<sub>2</sub>. *Phys. Rev. B: Condens. Matter Mater. Phys.* **2008**, *78*, 2–5.
- (4) Chen, G. F.; Li, Z.; Wu, D.; Li, G.; Hu, W. Z.; Dong, J.; Zheng, P.; Luo, J. L.; Wang, N. L. Superconductivity at 41 K and its competition with spin-density-wave instability in layered CeO<sub>1-x</sub>FeAs. *Phys. Rev. Lett.* **2008**, *100*, 1–4.
- (5) Yeom, H.; Takeda, S.; Rotenberg, E.; Matsuda, I.; Horikoshi, K.; Schaefer, J.; Lee, C.; Kevan, S.; Ohta, T.; Nagao, T.; Hasegawa, S. Instability and Charge Density Wave of Metallic Quantum Chains on a Silicon Surface. *Phys. Rev. Lett.* **1999**, *82*, 4898–901.
- (6) Borodin, D.; Zaitsev-Zotov, S. V.; Nad, F. Y. Coherence of a charge density wave and phase slip in small samples of a quasi-one-dimensional conductor TaS<sub>3</sub>. *Sov. Phys. JETP* **1987**, *66*, 793–802.
- (7) Bourne, L. C.; Zettl, A. Elastic Anomalies in the charge density wave conductor K<sub>0.3</sub>MoO<sub>3</sub>. *Solid State Commun.* **1986**, *60*, 789–92.
- (8) Friend, R. H.; Yoffe, A. D. Electronic properties of intercalation complexes of the transition metal dichalcogenides. *Adv. Phys.* **1987**, *36*, 1–94.
- (9) Wilson, J. A.; Di Salvo, F. J.; Mahajan, S. Charge density waves and superlattices in metallic layered transition-metal dichalcogenides. *Adv. Phys.* **1975**, *24*, 117–201.
- (10) Sipos, B.; Kusmartseva, A. F.; Akrap, A.; Berger, H.; Forró, L.; Tutis, E. From Mott state to superconductivity in 1T-TaS<sub>2</sub>. *Nat. Mater.* **2008**, *7*, 960–5.
- (11) Fazekas, P.; Tosatti, E. Charge carrier localization in pure and doped 1T-TaS<sub>2</sub>. *Physica B+C* **1980**, *99*, 183–187.
- (12) Di Salvo, F. J.; Graebner, J. E. The low temperature electrical properties of 1T-TaS<sub>2</sub>. *Solid State Commun.* **1977**, *23*, 825–8.
- (13) Clerc, F.; Bovet, M.; Berger, H.; Despont, L.; Koitzsch, C.; Gallus, O.; Patthey, L.; Shi, M.; Krempasky, J.; Garnier, M. G.; Aebi, P. Spin-orbit splitting in the valence bands of 1T-TaS<sub>2</sub> and 1T-TaSe<sub>2</sub>. *J. Phys.: Condens. Matter* **2004**, *16*, 3271.
- (14) Smith, N. V.; Kevan, S. D.; DiSalvo, F. J. Band structures of the layer compounds 1T-TaS<sub>2</sub> and 2H-TaSe<sub>2</sub> in the presence of commensurate charge-density waves. *J. Phys. C: Solid State Phys.* **1985**, *18*, 3175–89.
- (15) Hollander, M. J.; Liu, Y.; Lu, W. J.; Li, L. J.; Sun, Y. P.; Robinson, J. A.; Datta, S. Electrically driven reversible insulator-metal phase transition in 1T-TaS<sub>2</sub>. *Nano Lett.* **2015**, *15*, 1861–6.
- (16) Petersen, J. C.; Kaiser, S.; Dean, N.; Simoncig, A.; Liu, H. Y.; Cavalieri, A. L.; Cacho, C.; Turcu, I. C. E.; Springate, E.; Frassetto, F.; Poletto, L.; Dhessi, S. S.; Berger, H.; Cavalleri, A. Clocking the melting transition of charge and lattice order in 1T-TaS<sub>2</sub> with ultrafast extreme-ultraviolet angle-resolved photoemission spectroscopy. *Phys. Rev. Lett.* **2011**, *107*, 1–5.
- (17) Ang, R.; Tanaka, Y.; Ieki, E.; Nakayama, K.; Sato, T.; Li, L. J.; Lu, W. J.; Sun, Y. P.; Takahashi, T. Real-space coexistence of the melted Mott state and superconductivity in Fe-substituted 1T-TaS<sub>2</sub>. *Phys. Rev. Lett.* **2012**, *109*, 1–5.
- (18) Ang, R.; Miyata, Y.; Ieki, E.; Nakayama, K.; Sato, T.; Liu, Y.; Lu, W. J.; Sun, Y. P.; Takahashi, T. Superconductivity and bandwidth-controlled Mott metal-insulator transition in 1T-TaS<sub>2</sub>-xSex. *Phys. Rev. B: Condens. Matter Mater. Phys.* **2013**, *88*, 1–5.
- (19) Svetin, D.; Vaskivskyi, I.; Sutar, P.; Goreschnik, E.; Gospodarcic, J.; Mertelj, T.; Mihailovic, D. Transitions between photoinduced macroscopic quantum states in 1T-TaS<sub>2</sub> controlled by substrate strain. *Appl. Phys. Express* **2014**, *7*, 103201.
- (20) Liu, G.; Debnath, B.; Pope, T. R.; Salguero, T. T.; Lake, R. K.; Balandin, A. A. A charge-density-wave oscillator based on an integrated tantalum disulfide–boron nitride–graphene device operating at room temperature. *Nat. Nanotechnol.* **2016**, *11*, 845–50.
- (21) Ryu, S.; Liu, L.; Berciaud, S.; Yu, Y. J.; Liu, H.; Kim, P.; Flynn, G. W.; Brus, L. E. Atmospheric oxygen binding and hole doping in deformed graphene on a SiO<sub>2</sub> substrate. *Nano Lett.* **2010**, *10*, 4944–51.
- (22) Tsen, A. W.; Hovden, R.; Wang, D.; Kim, Y. D.; Okamoto, J.; Spoth, K. a.; Liu, Y.; Lu, W.; Sun, Y.; Hone, J. C.; Kourkoutis, L. F.; Kim, P.; Pasupathy, A. N. Structure and control of charge density waves in two-dimensional 1T-TaS<sub>2</sub>. *Proc. Natl. Acad. Sci. U. S. A.* **2015**, *112*, 15054–9.
- (23) Nakanishi, K.; Shiba, H. Theory of Three-Dimensional Orderings of Charge Density Waves in 1T-TaX<sub>2</sub> (X:S, Se). *J. Phys. Soc. Jpn.* **1984**, *53*, 1103–13.
- (24) Yu, Y.; Yang, F.; Lu, X. F.; Yan, Y. J.; Cho, Y.-H.; Ma, L.; Niu, X.; Kim, S.; Son, Y.-W.; Feng, D.; Li, S.; Cheong, S.-W.; Chen, X. H.; Zhang, Y. Gate-tunable phase transitions in thin flakes of 1T-TaS<sub>2</sub>. *Nat. Nanotechnol.* **2015**, *10*, 270–6.
- (25) Samnakay, R.; Wickramaratne, D.; Pope, T. R.; Lake, R. K.; Salguero, T. T.; Balandin, A. A. Zone-folded phonons and the commensurate-incommensurate charge-density-wave transition in 1T-TaSe <math>\langle \infty > 2</math> thin films. *Nano Lett.* **2015**, *15*, 2965–2973.
- (26) Darancet, P.; Millis, A. J.; Marianetti, C. A. Three-dimensional metallic and two-dimensional insulating behavior in octahedral tantalum dichalcogenides. *Phys. Rev. B: Condens. Matter Mater. Phys.* **2014**, *90*, 2–6.
- (27) Neto, A. H. C.; Novoselov, K. New directions in science and technology: two-dimensional crystals. *Rep. Prog. Phys.* **2011**, *74*, 082501.
- (28) Castellanos-Gomez, A.; Roldán, R.; Cappelluti, E.; Buscema, M.; Guinea, F.; van der Zant, H. S. J.; Steele, G. A. Local Strain Engineering in Atomically Thin MoS<sub>2</sub>. *Nano Lett.* **2013**, *13*, 5361–6.
- (29) Desai, S. B.; Seol, G.; Kang, J. S.; Fang, H.; Battaglia, C.; Kapadia, R.; Ager, J. W.; Guo, J.; Javey, A. Strain-Induced Indirect to Direct Bandgap Transition in Multi layer WSe<sub>2</sub>. *Nano Lett.* **2014**, *14*, 4592–7.
- (30) Yang, S.; Wang, C.; Sahin, H.; Chen, H.; Li, Y.; Li, S. S.; Suslu, A.; Peeters, F. M.; Liu, Q.; Li, J.; Tongay, S. Tuning the optical, magnetic, and electrical properties of ReSe<sub>2</sub> by nanoscale strain engineering. *Nano Lett.* **2015**, *15*, 1660–6.
- (31) Pereira, V. M.; Castro Neto, A. H. Strain Engineering of Graphene's Electronic Structure. *Phys. Rev. Lett.* **2009**, *103*, 1–4.
- (32) Fei, R.; Yang, L. Strain-engineering the anisotropic electrical conductance of few-layer black phosphorus. *Nano Lett.* **2014**, *14*, 2884–9.
- (33) Pan, W.; Xiao, J.; Zhu, J.; Yu, C.; Zhang, G.; Ni, Z.; Watanabe, K.; Taniguchi, T.; Shi, Y.; Wang, X. Biaxial compressive strain engineering in graphene/boron nitride heterostructures. *Sci. Rep.* **2012**, *2*, 893.
- (34) He, X.; Li, H.; Zhu, Z.; Dai, Z.; Yang, Y.; Yang, P.; Zhang, Q.; Li, P.; Schwingenschlogl, U.; Zhang, X. Strain engineering in monolayer WS<sub>2</sub>, MoS<sub>2</sub>, and the WS<sub>2</sub>/MoS<sub>2</sub> heterostructure. *Appl. Phys. Lett.* **2016**, *109*, 173105.
- (35) Liu, Y.; Ang, R.; Lu, W. J.; Song, W. H.; Li, L. J.; Sun, Y. P. Superconductivity induced by Se-doping in layered charge-density-wave system 1T-TaS<sub>2</sub>-xSex. *Appl. Phys. Lett.* **2013**, *102*, 192602.
- (36) Albertini, O. R.; Zhao, R.; McCann, R. L.; Feng, S.; Terrones, M.; Freericks, J. K.; Robinson, J. A.; Liu, A. Y. Zone-center phonons of bulk, few-layer, and monolayer 1T-TaS<sub>2</sub>: Detection of the commensurate charge density wave phase through Raman scattering. *Phys. Rev. B: Condens. Matter Mater. Phys.* **2016**, *93*, 1–7.
- (37) Goli, P.; Khan, J.; Wickramaratne, D.; Lake, R. K.; Balandin, A. A. Charge density waves in exfoliated films of van der waals materials: Evolution of raman spectrum in TiSe<sub>2</sub>. *Nano Lett.* **2012**, *12*, 5941–5.
- (38) Blöchl, P. E. Projector augmented-wave method. *Phys. Rev. B: Condens. Matter Mater. Phys.* **1994**, *50*, 17953–79.



- (39) Kresse, G. From ultrasoft pseudopotentials to the projector augmented-wave method. *Phys. Rev. B: Condens. Matter Mater. Phys.* **1999**, *59*, 1758–1775.
- (40) Perdew, J. P.; Burke, K.; Ernzerhof, M. Generalized Gradient Approximation Made Simple. *Phys. Rev. Lett.* **1996**, *77*, 3865–8.
- (41) Johannes, M.; Mazin, I. Fermi surface nesting and the origin of charge density waves in metals. *Phys. Rev. B: Condens. Matter Mater. Phys.* **2008**, *77*, 165135.
- (42) Brouwer, R.; Jellinek, F. The low-temperature superstructures of 1T-TaSe<sub>2</sub> and 2H-TaSe<sub>2</sub>. *Physica B+C* **1980**, *99*, 51–5.
- (43) Wang, Y.; Wang, W. Y.; Chen, L. Q.; Liu, Z. K. Bonding charge density from atomic perturbations. *J. Comput. Chem.* **2015**, *36*, 1008–14.
- (44) Duffey, J. R.; Coleman, R. V. Raman Scattering from 1T-TaS<sub>2</sub>. *Solid State Commun.* **1976**, *20*, 617–621.
- (45) Yoshida, M.; Zhang, Y.; Ye, J.; Suzuki, R.; Imai, Y.; Kimura, S.; Fujiwara, A.; Iwasa, Y. Controlling charge-density-wave states in nanothick crystals of 1T-TaS<sub>2</sub>. *Sci. Rep.* **2015**, *4*, 7302.
- (46) Grüner, G. The dynamics of charge-density waves. *Rev. Mod. Phys.* **1988**, *60*, 1129–81.
- (47) Sohr, C.; Stange, A.; Bauer, M.; Rosnagel, K. How fast can a Peierls-Mott insulator be melted? *Faraday Discuss.* **2014**, *171*, 243–57.
- (48) Case, F. C. Modifications in the phase transition properties of predeposited VO<sub>2</sub> films. *J. Vac. Sci. Technol., A* **1984**, *2*, 1509.
- (49) Shao, D. F.; Xiao, R. C.; Lu, W. J.; Lv, H. Y.; Li, J. Y.; Zhu, X. B.; Sun, Y. P. Manipulating charge density waves in 1T-TaS<sub>2</sub> by charge-carrier doping: A first-principles investigation. *Phys. Rev. B: Condens. Matter Mater. Phys.* **2016**, *94*, 1–9.
- (50) Jin, W.; Yeh, P. C.; Zaki, N.; Zhang, D.; Liou, J. T.; Sadowski, J. T.; Barinov, A.; Yablonskikh, M.; Dadap, J. I.; Sutter, P.; Herman, I. P.; Osgood, R. M. Substrate interactions with suspended and supported monolayer MoS<sub>2</sub>: Angle-resolved photoemission spectroscopy. *Phys. Rev. B: Condens. Matter Mater. Phys.* **2015**, *91*, 1–6.
- (51) Shin, B. G.; Han, G. H.; Yun, S. J.; Oh, H. M.; Bae, J. J.; Song, Y. J.; Park, C.-Y.; Lee, Y. H. Indirect Bandgap Puddles in Monolayer MoS<sub>2</sub> by Substrate-Induced Local Strain. *Adv. Mater.* **2016**, *28*, 9378–9384.
- (52) Gruner, G.; Zettl, A. Charge density wave conduction: A novel collective transport phenomenon in solids. *Phys. Rep.* **1985**, *119*, 117–232.
- (53) Wilson, J. A.; Di Salvo, F. J.; Mahajan, S. Charge-density waves and superlattices in the metallic layered transition metal dichalcogenides. *Adv. Phys.* **1975**, *24*, 117–201.
- (54) Salvetti, G.; Roucau, C.; Ayroles, R.; Mutka, H.; Molinié, P. Defected structural modulation in the charge density wave compounds 1T-TaS<sub>2</sub> and 1T-TaSe<sub>2</sub>. *J. Phys., Lett.* **1985**, *46*, 507–11.
- (55) Fukuyama, H.; Lee, P. A. Dynamics of the charge-density wave. I. Impurity pinning in a single chain. *Phys. Rev. B: Condens. Matter Mater. Phys.* **1978**, *17*, 535–41.
- (56) Thorne, R. E.; McCarten, J. Thorne and McCarten reply. *Phys. Rev. Lett.* **1990**, *65*, 272–3.
- (57) Lee, P. A.; Fukuyama, H. Dynamics of the charge-density wave. II. Long-range Coulomb effects in an array of chains. *Phys. Rev. B: Condens. Matter Mater. Phys.* **1978**, *17*, 542–8.
- (58) Shukla, N.; Thathachary, A. V.; Agrawal, A.; Paik, H.; Aziz, A.; Schlom, D. G.; Gupta, S. K.; Engel-Herbert, R.; Datta, S. A steep-slope transistor based on abrupt electronic phase transition. *Nat. Commun.* **2015**, *6*, 7812.